A Prototype Algorithm for All-Sky Atmospheric Temperature Profile Retrieval over Ocean Based on Channel Optimization for the FY-4M Satellite

Yu Wang[1,2], Xinbin Ma[1], Banghai Wu[3], Qiang Guo[4], Jing Xi[1,2], Rui Li[1], Xin Wang[4], Xiaoqing Li[4]

[1]School of Earth and Space Sciences, Joint Laboratory of Fengyun Remote Sensing, University of Science and Technology of China, Hefei, 230026, China
[2]China Meteorological Administration Xiong'an Atmospheric Boundary Layer Key Laboratory, Xiong'an New Area, Baoding, 071800, China
[3]Aviation Industry Corporation of China Leihua Electronic Technology Institute, Wuxi, 214063, China
[4]National Satellite Meteorological Center (National Center for Space Weather), China Meteorological Administration, Beijing, 100081, China

Correspondence to: Jing Xi (xij1994@ustc.edu.cn)

Abstract. As the world's first geostationary satellite equipped with a passive microwave payload, China's FengYun-4M (FY-4M) is planned to be launched at the end of 2026, ushering in a new era of continuous observation of various geophysical parameters associated with weather processes. To better understand the observational characteristics of this satellite's more than a hundred channels, especially the potential application of its unique temperature hyperspectral channels (52.6-57.3 GHz) and several high-frequency channels (380 and 424 GHz) in the high-precision detection of atmospheric temperature profiles over ocean, this paper proposes a complete retrieval algorithm with a channel optimization scheme, based on information entropy theory and the Bayesian technique. Using degrees of freedom as an indicator, the ranking results of information contribution show that when hyperspectral channels are included, water vapor absorption channels and window channels used to obtain auxiliary information such as water vapor and hydrometeors are more important for the quantitative extraction of temperature profile information than traditional oxygen absorption channels at 50 GHz and 118 GHz. Based on this, a corresponding channel configuration was constructed for all-weather temperature profile retrieval. The results of retrieval experiments show that the root mean square error (RMSE) remains below 0.5 K under clear-sky and cloudy conditions, and is within 0.8 K during precipitation. Additionally, the computational time is reduced by 14% relative to the full-channel configuration. This suggests that the presented algorithm with this channel configuration scheme is able to achieve a favorable balance between retrieval accuracy and computational efficiency, making it a preferred choice for future operational retrieval systems.

1 Introduction

The atmospheric temperature profile is a key parameter for characterizing the thermodynamic state of the atmosphere, which is essential for understanding weather processes, assessing climate change, and implementing various meteorological support

tasks (Zhang et al., 2024). Furthermore, it serves as a critical component of the global observing system for numerical weather prediction, significantly contributing to the accuracy of weather forecasts (Yan et al., 2020; Wang et al., 2021; Xue et al., 2022).

Among various techniques for observing the atmospheric vertical thermal structure, spaceborne passive microwave (PMW) remote sensing has the advantages of all-sky and large-scale observation, utilizing the dependence of oxygen absorption on frequency and atmospheric temperature. Near an oxygen absorption band, channels closer to the center line generally have larger absorption coefficients and optical depths, so radiative contributions from the lower atmosphere and surface are more strongly attenuated. As a result, these channels are mainly sensitive to radiation from higher atmospheric layers, leading to higher peak altitudes of their temperature weighting functions (Rodgers, 2000; Aires et al., 2015). Meanwhile, warmer atmospheric layers emit stronger microwave radiation. There are currently numerous spaceborne microwave temperature sounders equipped with the 50-60 GHz oxygen absorption band, including the Microwave Sounding Unit (MSU) deployed on the National Oceanic and Atmospheric Administration (NOAA) series satellites (Mo et al., 2001), and the Advanced Technology Microwave Sounder (ATMS) onboard the Suomi National Polar-orbiting Partnership (Suomi-NPP) and Joint Polar Satellite System (JPSS) satellites from the United States (Weng et al., 2013), as well as the Micro-Wave Temperature Sounder-2 (MWTS-2) carried by FengYun-3C (FY-3C) and FengYun-3D (FY-3D) satellites from China (Zhang et al., 2022). In addition, China has taken the lead in using the 118 GHz oxygen absorption band on instruments such as the Micro-Wave Humidity Sounder-2 (MWHS-2) onboard the FY-3 series satellites for vertical atmospheric temperature profiling (Lawrence et al., 2017). The oxygen absorption line at this frequency is nearly symmetric and isolated from other lines, so that the negligible overlapping effect allows for simplifying atmospheric transmittance modeling (Gasiewski et al., 1990; Tretyakov et al., 2001). It should be noted that due to hardware design constraints such as antenna size, these microwave sounders are exclusively deployed on polar-orbiting satellites, operating at altitudes of 400-800 km. The sampling frequency of twice per day is insufficient for continuous regional observation, which limits the application of retrieved temperature profiles in weather monitoring and data assimilation (Lambrigtsen et al., 2016).

Developing PMW payloads onboard geostationary satellite with the unique capability of large-scale and high-frequency observations is an effective way to address the aforementioned observational bottlenecks, which is of great significance for monitoring and nowcasting rapidly evolving weather systems (Christensen et al., 2007). In fact, several countries have launched development programs for PMW instruments in geostationary orbit, including the Geostationary Synthetic Thinned-Aperture Radiometer (GeoSTAR) concept proposed by the United States (Lambrigtsen et al., 2007) and the Geostationary Atmospheric Sounder (GAS) project developed in Europe (Christensen et al., 2007). In comparison, China has made the fastest progress. A prototype based on a large real-aperture antenna scheme has already been developed (Xie et al., 2018a, b), and the formal instrument will be onboard the FengYun-4M (FY-4M) satellite, which is scheduled to be launched at the end of 2026. As the world's first geostationary PMW payload used for operational purpose, it would usher in a new era of Earth observation. It is worth mentioned that this instrument is equipped with 135 channels, far exceeding the channel numbers of existing spaceborne PMW sensors. Among them, 89 hyperspectral channels located in the 52.6-57.3 GHz

oxygen absorption band (Bi et al., 2024), together with several high-frequency channels in the millimeter to submillimeter wavebands, are being used for the first time worldwide in spaceborne instruments. This makes precise observations of vertical temperature structure and solid hydrometeor possible. Chen et al. (2024, 2025) conducted observing system simulation experiments for the FY-4M satellite, confirming that the assimilation of its observational data has a positive impact on typhoon forecasting due to the high temporal resolution. Specifically, measurements in the oxygen and water vapor absorption bands can respectively contribute to improvements in typhoon track and intensity predictions.

However, the high-frequency and multi-band observation characteristics of the FY-4M satellite also introduce new challenges to the subsequent retrieval of various physical parameters. The minimum observation interval of approximately 3 minutes imposes stringent requirements on the computational complexity of operational algorithms, especially considering that using more channels generally increases computational cost and the accumulation of observation errors. In fact, among these 135 channels, information redundancy may exist within certain channel subsets. In addition, the effectiveness of measurements from those channels being used for the first time in the retrieval of key geophysical variables is still unknown. In order to achieve a balance between computational efficiency and accuracy, therefore, channel selection tailored to specific retrieval objectives is essential for the FY-4M satellite. Generally, existing channel selection methods are primarily based on weighting functions (He et al., 2015) or information content (IC) analysis (Rodgers, 1998; Sahoo et al., 2015). The former selects channels by quantifying their sensitivity to atmospheric parameters at different altitudes, but fails to fully account for the impacts of instrument noise and background errors (Zhou et al., 2024). In comparison, as a more comprehensive technique, the IC analysis focuses on the retrieval capability of the channels with full consideration of noise effects, quantifying the independent IC of each channel or combination of channels, thereby only retaining the channels that maximize IC while discarding those with little or redundant information (Bi et al., 2024; Rodgers, 2000; Xiao and Weng, 2022).

It is noted that current few studies on channel sensitivity analysis for the FY-4M satellite generally focus on cloud-free scenarios. For instance, Bi et al. (2024) investigated the characteristics of hyperspectral channels under clear-sky condition and found that the most informative channels of temperature are mainly located near 57 GHz. In terms of non-hyperspectral channels, Xiao and Weng (2022) pointed out that high IC for atmospheric temperature is mainly obtained from 50-70 GHz, whereas that for water vapor comes from 183 GHz and 380 GHz. However, under cloudy and precipitating conditions, hydrometeors in various phases would exert significant scattering and absorption effects on microwave radiation (Mech et al., 2020), and in turn may affect the sensitivity and response of certain channels to some atmospheric parameters at different altitudes, leading to potential discrepancies in their retrieval capabilities compared to those under clear-sky condition.

Therefore, to gain a more comprehensive understanding of the characteristics of over a hundred channels for the FY-4M satellite, and to better use them for all-sky atmospheric temperature profile retrieval, in this study optimal channel selection under various weather conditions is investigated, employing an IC analysis based on the Jacobian matrix and degrees of freedom for signal (DFS). Also, the selected channels are further evaluated through temperature retrieval with the Bayesian algorithm. This paper is organized as follows: Section 2 introduces the FY-4M satellite, as well as the IC analysis and

retrieval methods. Section 3 presents the results of the channel optimization and the corresponding retrieval validation. Finally, Section 4 summarizes the main findings and outlines future perspectives.

2 Data and Methods

2.1 The FY-4M satellite

According to the plan, the FY-4M satellite will be positioned at 123.5°E, and the satellite zenith angles (SZAs) at each footprint within the satellite's field of view will vary from 0° to nearly 80° (Fig. 1). Note that the surface emissivity of different land types varies complexly with observation frequency and zenith angle (He et al., 2021), which has a significant impact on channel selection and retrieval performance. Unfortunately, although the land surface emissivity for some typical microwave channels can be obtained at certain observation angles under clear-sky and even cloudy but rainless conditions (Li et al., 2020; Li et al., 2022; Hu et al., 2026), there is still a lack of comprehensive understanding about the variations in surface emissivity for various land types across the entire SZA range and all channels of the FY-4M satellite. Therefore, to reduce the impact of surface emissivity settings on channel selection analysis, this study will focus only on the oceanic surface, where microwave properties are more homogeneous and emissivity is easier to calculate.

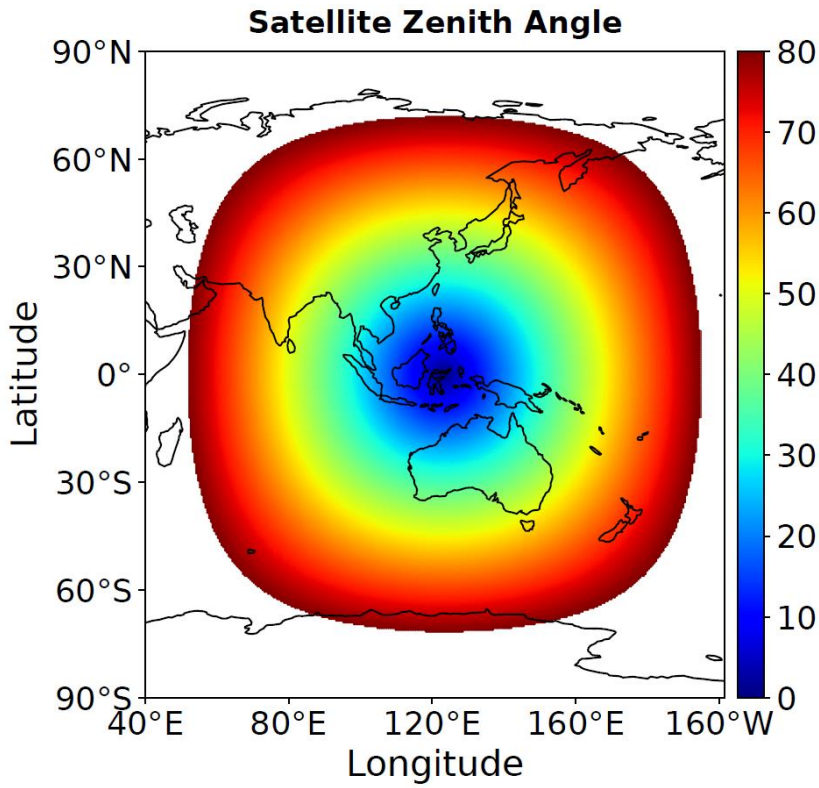

Figure 1. Distribution of SZAs of the FY-4M satellite within the observational coverage.

The PMW sounder onboard the FY-4M satellite has 135 observation channels, with frequencies ranging from 23 GHz to 425 GHz, as detailed in Table 1. The hyperspectral channels in the 52.6-57.3 GHz band are divided into two sub-bands, with spectral resolution of 200 MHz (52.6-55 GHz) and 30 MHz (55-57.3 GHz), respectively. This design is expected to offer significant potential for retrieving high-resolution atmospheric temperature profiles (Bi et al., 2024). As a good complement to hyperspectral channels, other non-hyperspectral oxygen absorption channels at 54 GHz, 118 GHz, and 425 GHz can also be used for temperature sounding. Among them, 54 GHz band is considered useful for capturing the temperature structure within a typhoon, while the 118 GHz and 425 GHz can provide temperature information for the middle and upper-middle layers of the atmosphere, respectively. Regarding the water vapor absorption bands, 23.8 GHz and 183 GHz are commonly implemented on existing PMW payloads, such as the MicroWave Radiation Imager for the Rainfall Mission (MWRI-RM) onboard the FY-3G satellite (He et al., 2024; Zhang et al., 2023), whereas the 380 GHz band is uniquely available on the FY-4M satellite. Additionally, the 31.4 GHz, 89 GHz, 166 GHz, and 229 GHz channels as window or quasi-window bands, can be used to effectively obtain information about the surface background and various hydrometeors (Xie et al., 2018a).

Table 1. Channel characteristics of the FY-4M satellite.

Band	Number	Frequency (GHz)	Bandwidth (MHz)	Polarization	Design Purpose
K/Ka	1	23.8	270	V	Total water vapor sounding
	2	23.8	270	H	
	3	31.4	180	V	Surface radiation correction
	4	31.4	180	H	
V	5	50.3	180	V	Atmospheric temperature profile sounding
	6	50.3	180	H	
	7	51.76	400	H	
	8	52.8	400	H	
	9	53.246±0.08	2*140	H	
	10	53.596±0.115	2*170	H	
	11	53.948±0.081	2*142	H	
	12	54.4	400	H	
	13	54.94	400	H	
	14	55.5	330	H	
	15	57.290334(f0)	330	H	
	16	f0±0.217	2*78	H	
	17	f0±0.322±0.048	4*36	H	
	18	f0±0.322±0.022	4*16	H	
	19	f0±0.322±0.01	4*8	H	
	20	f0±0.322±0.0045	4*3	H	
Hyperspectral	21-32	52.6-55	200	V	Hyperspectral atmospheric temperature profile sounding
	33-109	55-57.3	30	V	
W	110	89.0	3000	V	Surface radiation correction and ice cloud detection
F	111	118.75±0.08	2*20	H	Atmospheric temperature and humidity profile sounding
	112	118.75±0.2	2*100	H	
	113	118.75±0.3	2*165	H	
	114	118.75±0.8	2*200	H	
	115	118.75±1.1	2*200	H	
	116	118.75±2.5	2*200	H	
	117	118.75±3.0	2*1000	H	

	118	118.75±5.0	2*2000	H	
G	119	165.5	3000	V	Quasi-window channel
	120	183.31±11	2*2000	H	Mid-level atmospheric humidity profile sounding and ice cloud detection
	121	183.31±7	2*2000	H	
	122	183.31±4.5	2*2000	H	
	123	183.31±3	2*1000	H	
	124	183.31±1.8	2*1000	H	
	125	183.31±1	2*500	H	
J	126	229	2000	V	Experimental ice cloud remote sensing
Y1	127	380.197±18	2*2000	H	Atmospheric humidity profile sounding
	128	380.197±9	2*2000	H	
	129	380.197±1.5	2*500	H	
	130	380.197±0.4	2*200	H	
Y2	131	424.763±4	2*1000	H	Middle- and upper-level atmospheric temperature profile sounding
	132	424.763±1.5	2*600	H	
	133	424.763±1	2*400	H	
	134	424.763±0.6	2*200	H	
	135	424.763±0.3	2*100	H	

2.2. A priori database development

As the foundation for IC analysis and subsequent retrieval, a comprehensive and representative a priori database is essential. Such a database should encompass a wide range of geophysical parameters under diverse weather conditions, including vertical profiles of cloud liquid water content (CLWC), rain water content (RWC), ice water content (IWC), atmospheric temperature, relative humidity, and pressure, as well as auxiliary parameters such as surface precipitation rate (SPR), sea surface temperature (SST), 10 m wind speed (WS), surface emissivity, and the simulated brightness temperatures (TBs) for all channels of the FY-4M satellite. To construct this database, multiple sets of data for the entire year of 2015 were used, including the European Centre for Medium-Range Weather Forecasts (ECMWF) Reanalysis v5 (ERA5) (Hersbach et al., 2020) with a 1-hour temporal resolution and a 0.25° spatial resolution, the Global Precipitation Measurement (GPM) Microwave Imager (GMI) Level 1C-R Version 05 TB product (Wentz and Draper, 2016) and GMI Level 2 retrieval product (Version 07) derived via the Goddard profiling algorithm (GPROF) (Kummerow et al., 2015). Specifically, ERA5 was used to obtain atmospheric temperature, relative humidity, pressure, SST, and WS; the GMI L1C-R product provides observed TBs served as the observation vector in the subsequent one-dimensional variational (1D-Var) adjustment; and the GPROF L2 product supplies hydrometeor profiles, including CLWC, RWC, and IWC, as part of the a priori state vector, together with auxiliary precipitation information such as SPR. Here ERA5 gridded data were matched to GMI pixels using a nearest-

neighbour approach within the full-disk coverage of the FY-4M satellite, resulting in approximately 200 million collocated oceanic samples for the subsequent analysis and retrieval experiments.

For each sample in the a priori database, vertical profiles of atmospheric temperature, relative humidity, and pressure with 37 pressure levels ranging from 1000 hPa to 1 hPa, as well as SST and WS are directly obtained from ERA5 data. Moreover, the oceanic surface emissivity is calculated based on the SST and WS using the fast ocean surface emissivity model version 5 (FASTEM-5) (Bormann et al., 2012; Liu et al., 2011).

As the radiometric calibration standard for all radiometers in the GPM constellation, GMI has been in operation for over ten years, providing stable and reliable TB observations with frequencies ranging from 10.65 GHz to 183 GHz (Draper et al., 2015). In addition, the GPROF product provides SPR and vertical profiles of CLWC, RWC and IWC, with a vertical resolution of 0.5 km (1 km) below (above) 10 km. The horizontal resolution of both TB and GPROF products is approximately equivalent to the instantaneous field of view of the GMI 18.7 GHz channel (11 km × 18 km). Since a Bayesian probabilistic algorithm is used for temperature profiling retrieval in this study, the spatiotemporal distribution characteristics of various geophysical parameters in the a priori database should be as comprehensive and realistic as possible (Kummerow et al., 2006). Given the retrieval errors in GPROF products, a one-dimensional variational (1D-Var) method was used to adjust the retrieved hydrometeors following Yin and Liu (2017) and Wu et al. (2026), making their physical relationship with the observed TBs more consistent, thereby improving the reliability of the a priori database (Kummerow et al., 2011).

In the 1D-Var method, the discrepancy between a state vector ($\boldsymbol{x}$) and the observed GMI TB vector ($\boldsymbol{y}$) can be represented by the following cost function:

$$J(\boldsymbol{x}) = (\boldsymbol{x} - \boldsymbol{x_a})^T \boldsymbol{S_a^{-1}} (\boldsymbol{x} - \boldsymbol{x_a}) + (\boldsymbol{y} - H(\boldsymbol{x}))^T \boldsymbol{S_y^{-1}} (\boldsymbol{y} - H(\boldsymbol{x})) \tag{1}$$

where $\boldsymbol{x_a}$ is the a priori state vector, and $\mathrm{H}(\boldsymbol{x})$ is the simulated GMI TB vector calculated by a plane-parallel microwave radiative transfer (MWRT) model (Liu, 1998). The observation vector $\boldsymbol{y}$ includes TBs from nearly all GMI channels, except for the horizontally polarized channels at 89 GHz and 166 GHz. These channels are sensitive to oriented ice habits, which may not be accurately simulated by the MWRT model (Gong and Wu, 2017). It should be noted that this exclusion applies only to the GMI observation vector used in the 1D-Var adjustment of the a priori database and does not preclude the corresponding FY-4M frequency channels from being considered in the subsequent channel selection and retrieval experiments. $\boldsymbol{S_a}$ and $\boldsymbol{S_y}$ denote the background error covariance matrix and the observation error covariance matrix, respectively. In this study, both matrices were prescribed as static matrices. The standard deviations in $\boldsymbol{S_a}$ were specified according to the type of state variable. For hydrometeor contents, the standard deviation was set to 0.2 after the logarithmic transformation (base 10). For surface emissivity, the standard deviation was set to 0.5 after the inverse hyperbolic tangent (arctanh) transformation. $\boldsymbol{S_y}$ was calculated from the instrument noise of each GMI channel (Yin and Liu, 2017; Wu et al., 2026). Although error correlations may exist among different state variables and vertical layers, both matrices were treated

as diagonal matrices to improve computational efficiency and numerical stability. The minimization of the cost function was performed following Wu et al. (2026).

After obtaining the adjusted hydrometeor profiles, the MWRT model was used to simulate TBs for all channels of the FY-4M satellite with the pixel-dependent SZAs. Consequently, a comprehensive a priori dataset was constructed, consisting of the simulated TBs, multiple geophysical parameter profiles, and SZAs.

2.3. Information content analysis

According to information theory, a system reaches maximum entropy in a state of complete disorder, corresponding to minimum knowledge of its true state. The reduction in the system information entropy brought by observations is defined as the IC of the observations. This information gain is mainly reflected in reduced estimation error and enhanced system certainty (Xiao and Weng, 2022). Therefore, IC analysis allows us to evaluate retrieval errors without performing the actual retrieval. Using a standard IC analysis method (Rodgers, 1998, 2000), the IC of different channels is compared and ranked (Kummerow et al., 2022; Birman et al., 2017), enabling a quantitative assessment of each channel's contribution to the temperature profile retrieval system, and thus the optimal channels are determined.

In this method, the retrieval error covariance matrix $\boldsymbol{A}$ is expressed as follows:

$$\boldsymbol{A} = (\boldsymbol{B}^{-1} + \boldsymbol{H}^{\boldsymbol{T}}\boldsymbol{R}^{-\boldsymbol{1}}\boldsymbol{H})^{-1} \tag{2}$$

where $\boldsymbol{H}$ is the Jacobian matrix, $\boldsymbol{B}$ is the background error covariance matrix, and $\boldsymbol{R}$ denotes the observation error covariance matrix, which includes instrument noise $\boldsymbol{R_\varepsilon}$ and radiative transfer model errors $\boldsymbol{R_f}$. In this study, $\boldsymbol{B}$ is constructed from the a priori error standard deviations and a vertical error correlation matrix. Here, the standard deviation is set to 1 K, while vertical correlation matrix is modeled using a Gaussian function truncated at ±2 standard deviations, with a correlation length of 2 km at each altitude (Aires et al., 2015).

$\boldsymbol{R_\varepsilon}$ is calculated using the following equation:

$$\boldsymbol{R_\varepsilon} = \frac{(\boldsymbol{T_{receiver}} + \boldsymbol{T_{antenna}})}{\sqrt{\boldsymbol{Bw} \times \boldsymbol{t}}} \tag{3}$$

where $\boldsymbol{T_{receiver}} = 4.5 \times \boldsymbol{F}(\mathrm{GHz}) + 30$ represents the equivalent receiver noise temperature (Aires et al., 2015, 2019). The channel frequency $\boldsymbol{F}(\mathrm{GHz})$, antenna temperature $\boldsymbol{T_{antenna}}$, integration time $\boldsymbol{t}$, and channel bandwidth $\boldsymbol{Bw}$ are all set according to the specifications of the FY-4M satellite. Here, $\boldsymbol{t}$ denotes the dwell time for each channel.

The radiative transfer error covariance matrix $\boldsymbol{R_f}$ was constructed in two steps (Aires et al., 2015). First, the atmospheric and surface modeling error variances were estimated separately for each channel and stored as diagonal matrices, $\boldsymbol{R_{atm}}$ and $\boldsymbol{R_{surf}}$, respectively. $\boldsymbol{R_{atm}}$ is assumed to increase linearly with frequency and $\boldsymbol{R_{surf}}$ is defined as $\Delta\mathrm{e}\boldsymbol{T_s}\boldsymbol{\tau}^2$, where $\Delta\mathrm{e} = 0.01$ is the surface emissivity error, $\boldsymbol{T_s}$ is the surface temperature, and $\boldsymbol{\tau}$ is the atmospheric transmittance. Second, to represent the

spectral correlations of these errors, a Gaussian function truncated at ±2 standard deviations, with a correlation length of 1 GHz, was applied to these variance estimates to construct the final non-diagonal matrix $\boldsymbol{R_f}$.

Figure 2 shows the calculated $\boldsymbol{R_\varepsilon}$, $\boldsymbol{R_{atm}}$ and $\boldsymbol{R_{surf}}$ for each channel of the FY-4M satellite. Since higher absorption leads to lower atmospheric transmittance, $\boldsymbol{R_{surf}}$ shows strong dependence on the channel's absorption capability. As a result, window channels have larger $\boldsymbol{R_{surf}}$. For absorption channels, $\boldsymbol{R_{surf}}$ is larger for those located far from the absorption peaks than those closer to them.

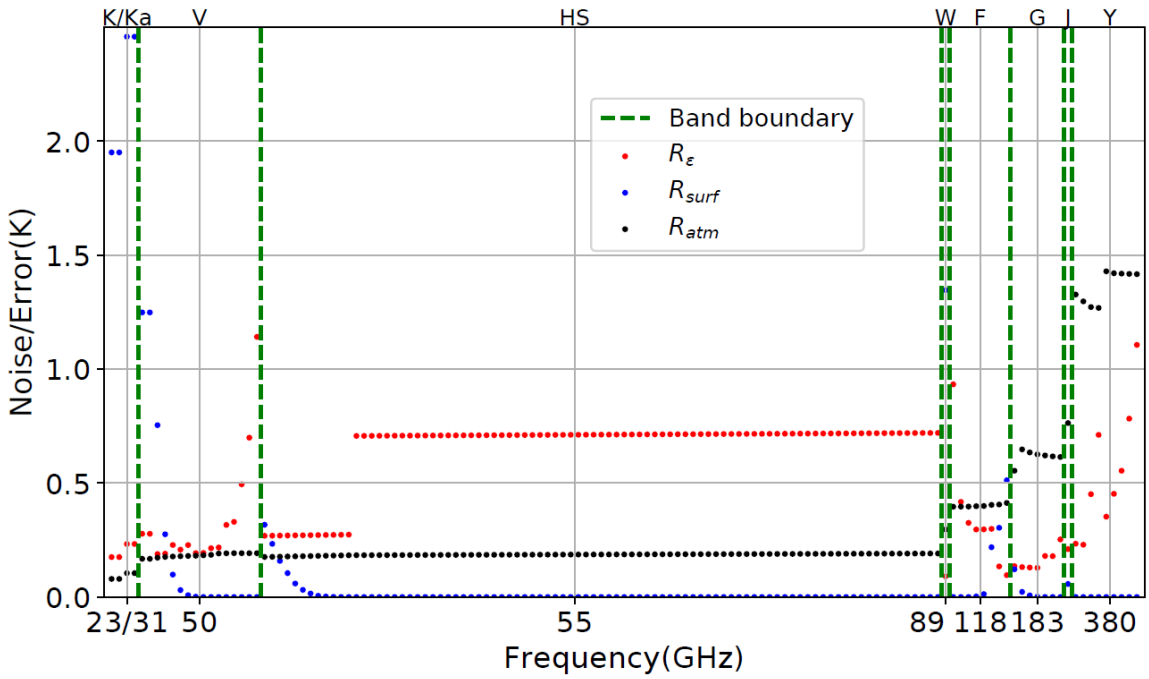

Figure 2. Instrument noise R_ε and radiative transfer errors induced by the atmosphere (R_{atm}) and surface (R_{surf}) for various channels of the FY-4M satellite. Green dashed lines indicate band boundaries.

To quantify the information contribution of each channel, the DFS is used as a metric (Mahfouf et al., 2015), and calculated by:

$$\mathrm{DFS} = Tr(\boldsymbol{I} - \boldsymbol{AB}^{-1}) \tag{4}$$

where $\boldsymbol{I}$ denotes the identity matrix, and Tr represents the trace operator. $\boldsymbol{A}$ and $\boldsymbol{B}$ denote the retrieval error covariance matrix and the background error covariance matrix, respectively. A higher DFS value indicates a larger contribution of the observation channel to the system state estimation. To select the optimal channel combination for retrieval, a sequential forward selection strategy is used. First, the DFS is calculated for each channel, and the channel with the highest DFS is

identified as the most informative channel, denoted as C1. Next, each of the remaining channels is combined with channel C1 to calculate the joint DFS. The channel that yields the maximum joint DFS is identified as the second largest channel, C2. This procedure is then repeated by combining the selected subset (e.g., C1 and C2) with the remaining channels to identify the third channel C3, and so forth, until all channels are ranked.

2.4. Bayesian retrieval method

As one of the dominant retrieval techniques in PMW remote sensing, the Bayesian retrieval algorithm combines the advantages of traditional statistical and physical retrieval methods, offering high computational efficiency and clear physical interpretability (Chedin et al., 1985; Evans et al., 1995; Kummerow et al., 2015). In this method, an a priori database consisting of the retrieved variables $\boldsymbol{x}$ and the corresponding TBs for multiple channels, which are typically coupled through radiative transfer calculation, is used to estimate prior and conditional probability distributions. Then, posterior probabilities are derived via Bayes' theorem and serve as the basis for the retrieval estimation. According to probability theory and the Bayesian formulation, the expected value of the retrieved parameter vector $E(\boldsymbol{x})$ for a given observation vector $\boldsymbol{y}$ can be expressed as:

$$E(\boldsymbol{x}) = \int_{0}^{+\infty} \boldsymbol{x} P(\boldsymbol{x}|\boldsymbol{y}) d\boldsymbol{x} = \int_{0}^{+\infty} \boldsymbol{x} \frac{P(\boldsymbol{y}|\boldsymbol{x})P(\boldsymbol{x})}{P(\boldsymbol{y})} dx \approx \frac{\sum_i \boldsymbol{x_i} P(\boldsymbol{y}|\boldsymbol{x_i})}{\sum_i P(\boldsymbol{y}|\boldsymbol{x_i})} \tag{5}$$

where $\boldsymbol{x_i}$ is the i-th state vector in the a priori database, representing the atmospheric temperature profile in this study. $\mathrm{P}(\boldsymbol{y}|\boldsymbol{x_i})$ is the conditional probability of the multi-channel observed TB vector $\boldsymbol{y}$ of the FY-4M satellite given $\boldsymbol{x_i}$, which is determined by the deviation between $\boldsymbol{y}$ and the simulated TBs by $H(\boldsymbol{x}_i)$. Assuming that this deviation is unbiased and follows a Gaussian distribution, the expected value can be expressed as:

$$E(\boldsymbol{x}) = \frac{\sum_i \boldsymbol{x_i} exp(-0.5[\boldsymbol{y} - H(\boldsymbol{x_i})]^T \boldsymbol{R^{-1}} [\boldsymbol{y} - H(\boldsymbol{x_i})])}{\sum_i exp(-0.5[\boldsymbol{y} - H(\boldsymbol{x_i})]^T \boldsymbol{R^{-1}} [\boldsymbol{y} - H(\boldsymbol{x_i})])} \tag{6}$$

where $\boldsymbol{R}$ is the error covariance matrix of observations. Here the observation vector includes TBs and SZAs, which serve as input variables for the retrieval of the temperature profile.

3 Results

To ensure the applicability and accuracy of the final temperature profile retrieval algorithm under all-sky conditions, the channel selection and retrieval performance evaluation will be separately conducted under different weather conditions, including clear-sky, cloudy, and precipitating. For each weather type, 1,000,000 samples were randomly selected from the aforementioned a priori database to perform IC analysis, and the corresponding mean temperature profiles are shown in Fig. 3. Although these profiles all show a similar vertical structure of decreasing with height across the three weather regimes,

their degrees of dispersion differ significantly. By comparison, temperature profiles under clear-sky condition have the greatest stability (Fig. 3a), while the variation is greatest on rainy days (Fig. 3c).

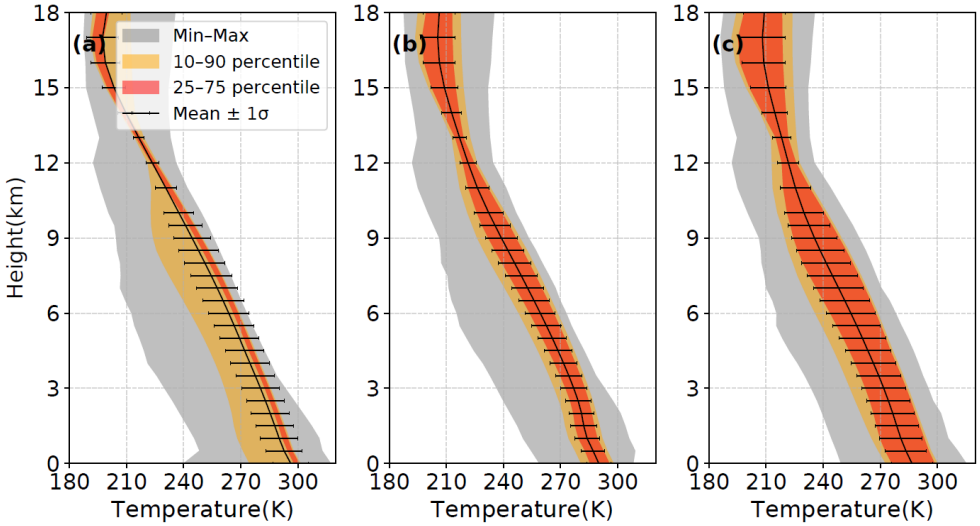

Figure 3. Temperature profiles used for IC analysis over the ocean under (a) clear-sky, (b) cloudy, and (c) precipitating conditions. The grey, yellow, and orange shading indicates the min-max, 10th-90th, and 25th-75th percentile ranges, respectively. The solid black line denotes the mean profile calculated from all samples under each weather condition, and the error bars represent the corresponding standard deviation.

Considering that the hyperspectral channels of the FY-4M satellite are planned to be used globally for the first time, their observational performance is still unknown. As a result, in this study the temperature detection capabilities of the hyperspectral channels and the remaining channels are investigated separately, in order to explore whether the former can provide incremental advantages in temperature profile detection.

Figure 4 first shows the atmospheric temperature Jacobians across all non-hyperspectral channels under various weather conditions. For each weather condition, the Jacobians were calculated separately for each of the 1,000,000 samples described above and then averaged. In clear-sky scenario (Fig. 4a), the 23 GHz band and the window channels are sensitive to near-surface atmosphere. Similarly, in some typical oxygen absorption bands of 54 GHz and 118 GHz, those channels located farther from the absorption peaks can also respond strongly to the near-surface layers, and the effective detection height gradually increases as the frequency approaches the corresponding absorption peak. Moreover, it is seen that the 424 GHz band is mainly sensitive to temperatures in the middle and upper atmosphere, which is consistent with the findings of Xiao and Weng (2022). Under cloudy and precipitating conditions (Figs. 4b and 4c), the distribution patterns of the Jacobians are basically similar to that in the clear-sky cases, but the response of the sounding channels near the 54 GHz and 118 GHz bands sensitive to the lower atmosphere is notably weakened, primarily due to the absorption and scattering effects of clouds and precipitation. Interestingly, some low frequency channels, such as 23.8 and 31.4 GHz, show relatively little change in

response to the lower atmosphere compared to clear-sky condition, which may be related to their great sensitivity to the emission effects of water vapor and liquid hydrometeors.

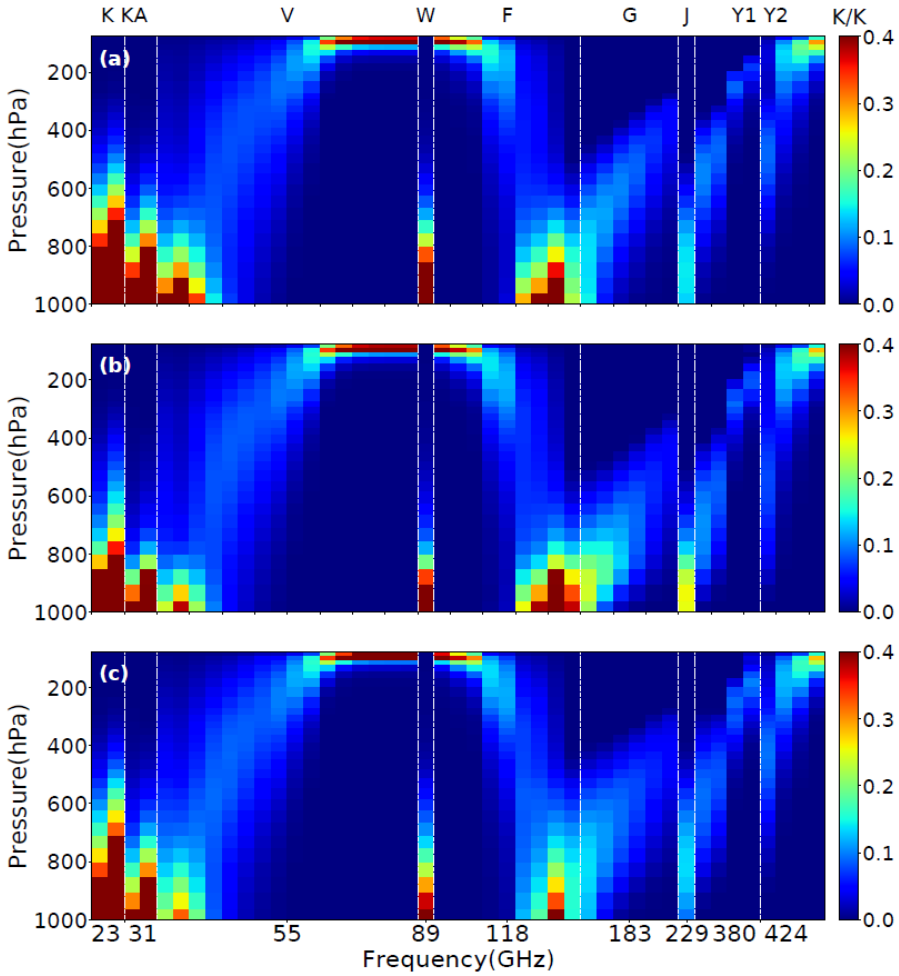

Figure 4. Temperature Jacobians for non-hyperspectral channels over the ocean under (a) clear, (b) cloudy, and (c) precipitating conditions.

By comparison, Figure 5 shows the spectral response of atmospheric temperature Jacobians for the hyperspectral band. Regardless of the weather conditions, the oxygen absorption coefficient generally increases with frequency across this range of 52.7-57 GHz. It is worth noting that this increase is not monotonic in detail, but exhibits some fluctuations due to the presence of secondary absorption peaks. Under clear-sky condition (Fig. 5a), the lower-frequency part of the hyperspectral band (near 52.7 GHz) with a lower absorption coefficient, can capture near-surface temperature information. As the frequency increases, the peak height gradually rises, but also experiences some fluctuations due to the influence of secondary absorption peaks. Compared with several other oxygen absorption bands in Fig. 4, hyperspectral channels have a stronger and more distinguishable capability to characterize the temperature stratification of the mid-to-upper atmosphere. Note that

this general trend is consistent with the findings of Aires et al. (2015), but the peak heights are not identical, which may be attributed to differences in data employed by the two studies. In Aires et al. (2015), a total of only 1,989 global atmospheric profiles in clear-sky scenes derived from the ECMWF forecasting system were used. In comparison, the data used in this study covers the whole coverage of the FY-4M satellite observations, and the larger data sample size allows for a more comprehensive display of the vertical temperature distribution characteristics of this region. Under cloudy and precipitating conditions (Figs. 5b and 5c), the lower-frequency channels (e.g., 53 GHz) far from the main absorption line show a weakened response near the surface due to the impact of clouds and precipitation on microwave signals, while the high-frequency channels associated with higher-altitude atmospheric temperatures are completely unaffected and show little difference from clear-sky condition. In summary, by utilizing some low-frequency channels sensitive to the lower atmosphere, combined with hyperspectral channels that can detect finer structures in the middle and upper atmosphere, it may be possible to obtain more complete temperature profile information across all vertical layers, even under cloudy and rainy conditions.

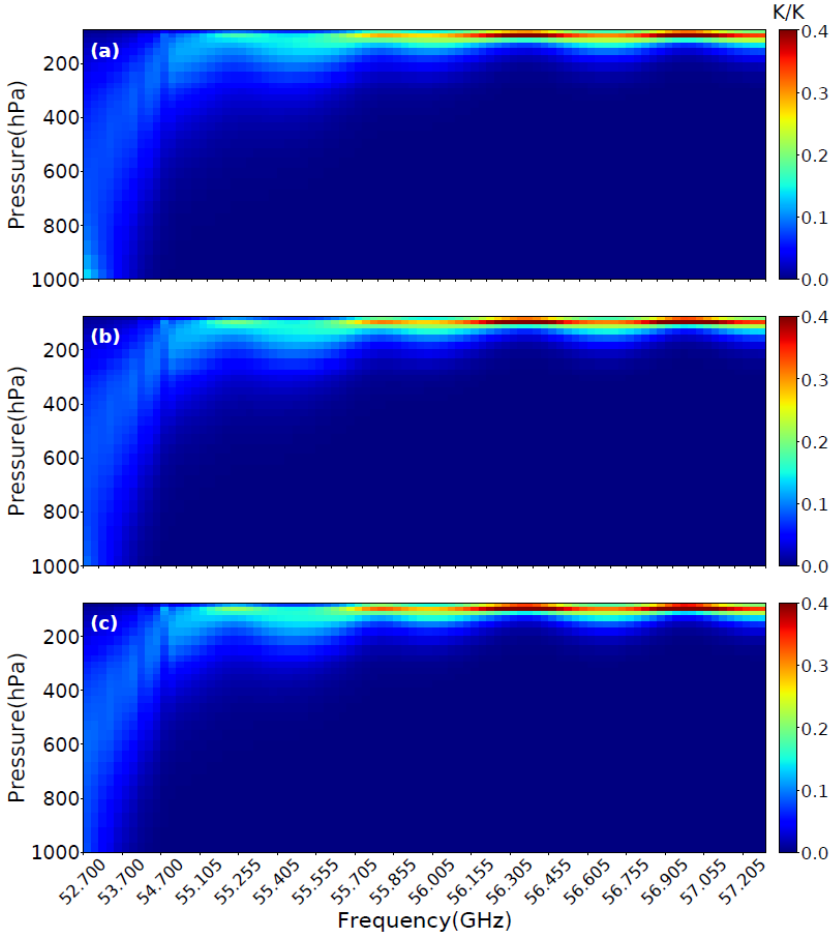

Figure 5. Similar to Fig. 4, but for hyperspectral channels.

In order to make the above channel combination strategy clearer, a more detailed evaluation and screening of each channel is carried out using the previously mentioned DFS calculation results. Figure 6 shows the joint IC for the non-hyperspectral channels, where the horizontal axis represents the channel frequencies ranked by DFS, while the vertical axis denotes the cumulative joint DFS.

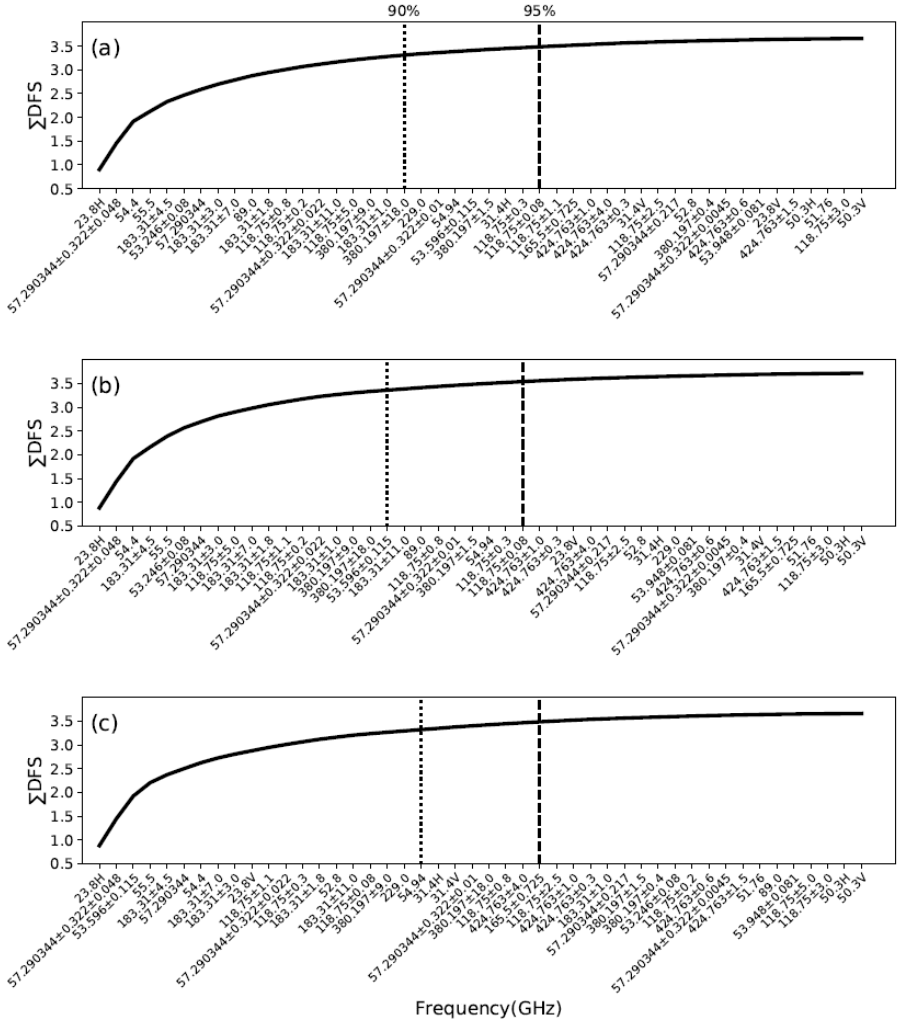

Figure 6. Independent rankings of non-hyperspectral channels over the ocean under (a) clear, (b) cloudy, and (c) precipitating conditions. The two dashed lines indicate the channel selection results corresponding to 90% and 95% of the total joint DFS of all channels, respectively.

Under clear-sky condition (Fig. 6a), the channels ranking high include not only those directly associated with oxygen absorption in the 50-60 GHz and 118 GHz bands that are sensitive to temperature information at various altitudes, but also water vapor sounding channels in the 23 GHz, 183 GHz, and 380 GHz bands, which can be attributed to the temperature dependence of water vapor absorption coefficient (Koshelev et al., 2021), thereby affecting the emitted radiation being

detected. For cloudy and precipitating scenarios (Figs. 6b and 6c), the performance of various channels is generally similar to that under clear-sky condition, except for the 89 GHz channel, whose ranking drops sharply. This is related to the fact that this window channel is in the transition zone between high and low frequencies, with complex emission and scattering effects. In clear-sky condition, the low atmospheric attenuation allows the measurements of this channel to be closely linked to the sea surface emission signal (Yang et al., 2024), whose variations are primarily determined by SST. This also leads to the inclusion of information from the lower atmospheric temperature with high IC ranking, which is highly correlated with SST due to air-sea heat exchange processes. With the appearance of clouds, however, the shorter wavelength makes this channel's penetration ability insufficient, and surface information is easily blocked by hydrometeors (Weng et al., 2003), resulting in a complete loss of near-surface temperature information. In addition, the liquid water emission signal of this channel is easily saturated, and the scattering effect of ice particles is more pronounced than at lower frequencies. All of this enhances the complexity of this channel's signal, and leads to a negligible contribution (approaching zero) to the joint DFS, especially in the presence of optically thick precipitating clouds.

Subsequently, a similar approach is adopted, but the entire set of hyperspectral channels is treated as a predefined 'super-channel' with the highest priority, and the sorting results of all channels for the FY-4M satellite are shown in Fig. 7. Similar to the results shown in Fig. 6, the growth rate of the joint DFS decreases as the number of channels increases and gradually levels off. However, a key difference is that once the hyperspectral channels are included, the highly-ranked non-hyperspectral channels are mainly window and water vapor absorption channels, rather than the oxygen absorption bands in the 50 GHz and 118 GHz. This suggests that hyperspectral channels are already capable of adequately capturing the primary information of the vertical distribution of atmospheric temperature, so that the complementary detection information needed for temperature retrieval is more focused on further constraints of humidity, near-surface states, and hydrometeors. For instance, water vapor channels such as 23 GHz and 183 GHz always rank among the top regardless of weather conditions. For window channels, the 89 GHz channel shows strong importance under clear-sky condition (Fig. 7a), similar to that shown in Fig. 6a, whereas the 31 GHz channel provides valuable hydrometeor information during precipitation (Fig. 7c), due to its high sensitivity to liquid water.

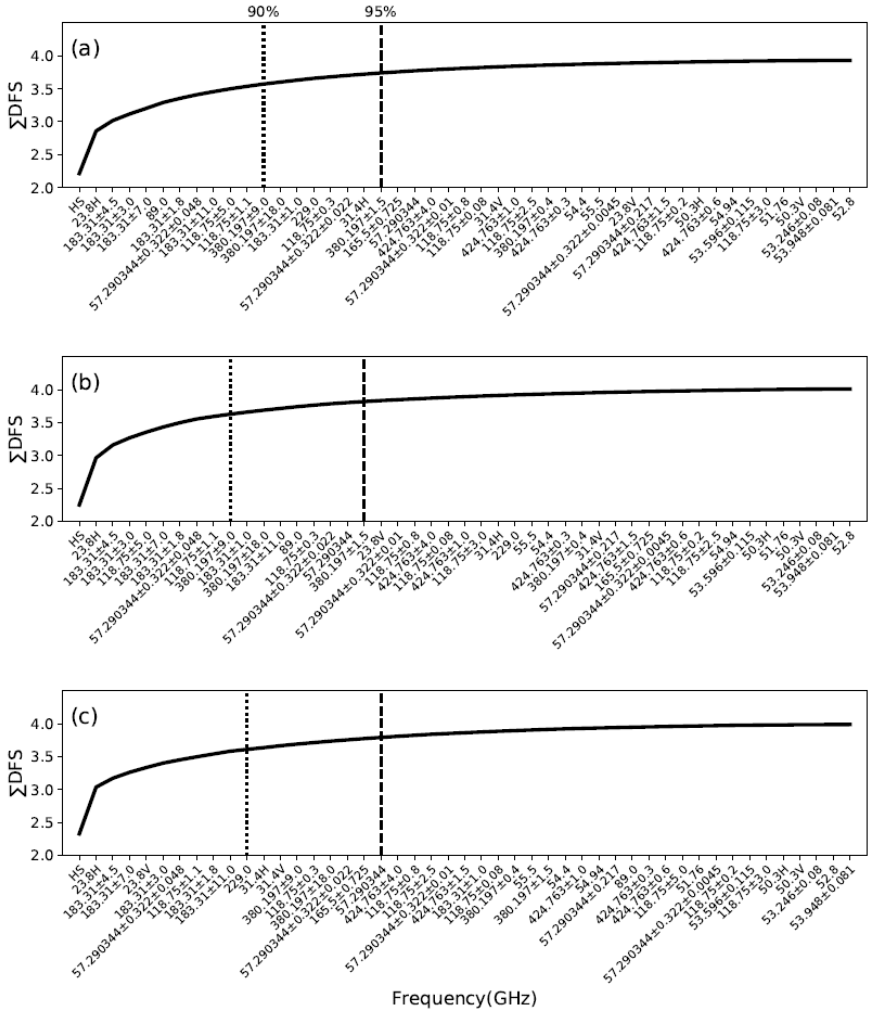

Figure 7. Similar to Fig. 6, but ranking all FY-4M channels, with the entire hyperspectral band (52.6-57.3 GHz) treated as a single predefined channel (HS) with the highest priority.

To ensure that the retrieval algorithm can maintain consistently high accuracy under all weather conditions after channel optimization, we separately extracted channel subsets that contribute 90% (or 95%) of the total joint DFS for different weather scenarios, and then took their union to construct channel configuration schemes adaptable to all-weather conditions, which are detailed in Table 2.

Table 2. Optimized channel configurations. NHC and AC denote the non-hyperspectral channel set and the complete FY-4M satellite channel set including hyperspectral bands, respectively. The suffixes 90 and 95 indicate the subsets contributing the top 90% and 95% of the joint DFS, respectively. A filled circle indicates that the channel is selected, while an open circle indicates it is not.

Frequency (GHz)	Polarization	NHC90	NHC95	AC90	AC95
Hyperspectral	V	○	○	●	●
23.8	V	●	●	●	●
23.8	H	●	●	●	●
31.4	V	○	●	○	●
31.4	H	○	●	○	●
50.3	V	○	○	○	○
50.3	H	○	○	○	○
51.76	H	○	○	○	○
52.8	H	●	●	○	●
53.246±0.08	H	●	●	○	○
53.596±0.115	H	●	●	○	○
53.948±0.081	H	○	○	○	○
54.4	H	●	●	○	○
54.94	H	●	●	○	○
55.5	H	●	●	○	○
57.290334(f0)	H	●	●	○	○
f0±0.217	H	○	○	○	○
f0±0.322±0.048	H	●	●	●	●
f0±0.322±0.022	H	●	●	○	●
f0±0.322±0.01	H	○	●	○	●
f0±0.322±0.0045	H	○	○	○	○
89.0	V	●	●	●	●
118.75±0.08	H	●	●	○	○
118.75±0.2	H	●	●	○	○
118.75±0.3	H	●	●	○	●
118.75±0.8	H	●	●	○	○
118.75±1.1	H	●	●	●	●
118.75±2.5	H	○	○	○	○
118.75±3.0	H	○	○	○	○
118.75±5.0	H	●	●	●	●
165.5	V	○	●	○	●
183.31±11	H	●	●	●	●
183.31±7	H	●	●	●	●
183.31±4.5	H	●	●	●	●
183.31±3	H	●	●	●	●
183.31±1.8	H	●	●	●	●
183.31±1	H	●	●	○	●
229	V	●	●	●	●
380.197±18	H	●	●	○	●
380.197±9	H	●	●	●	●
380.197±1.5	H	○	●	○	○
380.197±0.4	H	○	○	○	○

424.763±4	H	○	●	○	○
424.763±1.5	H	○	○	○	○
424.763±1	H	○	○	○	○
424.763±0.6	H	○	○	○	○
424.763±0.3	H	○	○	○	○

To evaluate the retrieval performance of different channel configuration schemes in the Bayesian algorithm, 100,000 samples each for clear-sky, cloudy, and precipitating conditions were randomly selected from the a priori database to form an independent test dataset, while the remaining samples were used as the training dataset. The corresponding atmospheric temperature profiles obtained from ERA5 in the a priori database for these test samples were used as the reference truth and compared with the Bayesian retrieval results for validation. To simulate instrumental noise, Gaussian random noise with a mean of 0 K and a standard deviation of 0.5 K was added to the simulated brightness temperatures of all FY-4M channels. In addition, retrieval results using the full set of channels of the FY-4M satellite are also provided as a reference.

The statistical distributions of temperature profile retrieval errors relative to the 'true values' in the a priori database for various channel configurations are shown in Fig. 8. For the non-hyperspectral observation system (Fig. 8a-c), regardless of weather conditions, the temperature bias profiles for different channel configuration schemes are generally distributed around the zero line, with root mean square error (RMSE) below 1 K. This indicates that the Bayesian algorithm can be effectively used for temperature profile retrieval, supported by a sufficiently comprehensive a priori database describing the variations of multiple geophysical parameters. In fact, by using a similar database and the Bayesian technique, multiple hydrometeor profiles for MWRI-RM of FY-3G satellite have also been accurately retrieved (Wu et al., 2026). On the other hand, it is reasonable that the use of all non-hyperspectral channels (NHC) with more abundant surface and atmospheric observation information leads to smaller uncertainties in retrieval results, compared to using only optimal channel subsets such as NHC90 and NHC95. For clear-sky scenes (Fig. 8a), the RMSE values of NHC95 and NHC90 increase by approximately 19% and 47% relative to the full NHC set, respectively. Especially as the height increases, the RMSEs of the two optimized channel configurations become larger compared to that of NHC. This is mainly because the differences among the three channel configurations are concentrated in several high-frequency channels above 300 GHz (Table 2), such as the 380 GHz water vapor channel and the 424 GHz oxygen band, which are primarily sensitive to the middle and upper atmosphere. In addition, NHC90 and NHC95 also have greater uncertainty in the low atmosphere, due to their lack of the 50 GHz wing-channels. In particular, the absence of the 31.4 GHz, which is highly sensitive to the near-surface layer (Fig. 4), further exacerbates the bias of NHC90.

Under cloudy condition (Fig. 8b), the uncertainties of all three channel configurations increase only slightly, except for the upper atmosphere, indicating that the effect of microwave emission from clouds on temperature profile retrieval can be effectively eliminated, even when only a subset of channels of the FY-4M satellite is used. Additionally, due to the shielding effect of clouds on the signals from the underlying surface, the extra 31.4 GHz channels in NHC95 compared to NHC90 at

this time mainly reflect the sensitivity to cloud water, providing better constraint ability, and in turn resulting in RMSE being closer to NHC. In comparison, with the occurrence of precipitation, the retrieval errors in various channel configuration schemes increase more noticeably, which may be due to the more complex scattering effects of precipitation particles and ice particles generated by convection, making it difficult to completely remove them through channel combination.

For observation system incorporating hyperspectral channels (Fig. 8d-f), it is unsurprisingly that the all-channel (AC) configuration exhibits the best overall performance, with mean temperature bias close to 0 and minimal RMSE on all layers. Compared with the NHC, the mean RMSE values under clear, cloudy, and precipitating conditions are reduced by 19%, 18%, and 11%, respectively. These results demonstrate that the design of hyperspectral channels for the FY-4M satellite makes it possible to obtain atmospheric temperature profiles more accurately under all-sky conditions. In clear-sky scenes (Fig. 8d), the RMSE values of optimal channel subsets of AC95 and AC90 increase by 17% and 45% compared to AC, respectively. With the appearance of clouds and precipitation, the differences between the subsets and the full set are reduced. Especially for precipitation cases, the retrieval performance of the three configurations is almost identical. This is because their differences are mainly concentrated in some typical oxygen absorption bands at 50-60, 118, and 424 GHz, whose contribution to temperature retrieval across the entire atmospheric layer cannot surpass, and may even be less than the hyperspectral channels used. Notably, the AC95 RMSE stays below 0.5 K in both clear-sky and cloudy scenes, and it is within 0.8 K even on rainy days, significantly outperforming the NHC configuration. These results further highlight the advantage of hyperspectral observations in improving the accuracy of atmospheric temperature sounding. Liu et al. (2026) reported temperature RMSEs of 3.07, 3.56, and 3.26 K for the FengYun-3E (FY-3E) vertical atmospheric sounding system (VASS) product under clear-sky, cloudy, and all-sky conditions, respectively, based on validation against radiosonde observations. The lower RMSEs obtained in the present study demonstrate the potential of the proposed algorithm. Considering the used plane-parallel MWRT model cannot fully represent three-dimensional scattering effects, however, the retrieval errors for real FY-4M observations may be larger than those indicated by the present simulation experiments. Therefore, the actual retrieval performance should be further evaluated using real on-orbit FY-4M observations in the future.

To further evaluate the retrieval performance under extreme weather conditions, moreover, the simulation results of Typhoon Doksuri at 25 July 2023 were used for a representative case study. The typhoon atmospheric fields were first simulated using the Weather Research and Forecasting (WRF) model, and treated as the reference truth. The corresponding FY-4M channel brightness temperatures were then calculated using the MWRT model and used as the input observations for the retrieval evaluation. As in the preceding simulation experiments, Gaussian random noise with a mean of 0 K and a standard deviation of 0.5 K was also added to represent instrumental noise. Fig. 9 shows the spatial distributions of the reference and retrieved temperature fields at 850, 500, and 250 hPa. Overall, the retrieved temperature fields reproduce the main spatial patterns of the reference fields at the three pressure levels. The warm-core structure near the typhoon center is clearly captured and the surrounding horizontal temperature gradients are also reasonably represented.

Fig. 10 further shows vertical profiles of temperature retrieval errors for different channel configuration schemes in the typhoon case. Except for the NHC90 scheme, the biases of the other schemes are still generally distributed around 0 K, with

RMSE values below 1 K at most vertical levels. This indicates that the proposed retrieval algorithm can maintain good performance even under strong convective weather conditions such as typhoons. Consistent with the results discussed above, the AC schemes generally show higher retrieval accuracy than the NHC schemes, with smaller RMSE values. This further highlights the important contribution of the hyperspectral channels to atmospheric temperature profile retrievals.

Table 3 shows the computational time required for retrieval under various channel configuration schemes. As more channels are used, the three configurations that include hyperspectral channels take longer, while achieving higher accuracy. Among them, the computational time for the AC95 is reduced by 14% compared with the AC, while maintaining a high level of retrieval accuracy. It should be noted that this reduction in computational time mainly comes from the retrieval phase. The AC95 scheme uses fewer channels in brightness temperature matching and probability calculation, thereby reducing the computational cost of each retrieval while preserving retrieval accuracy. Therefore, AC95 is recommended as the top priority choice of channel configuration in operational system.

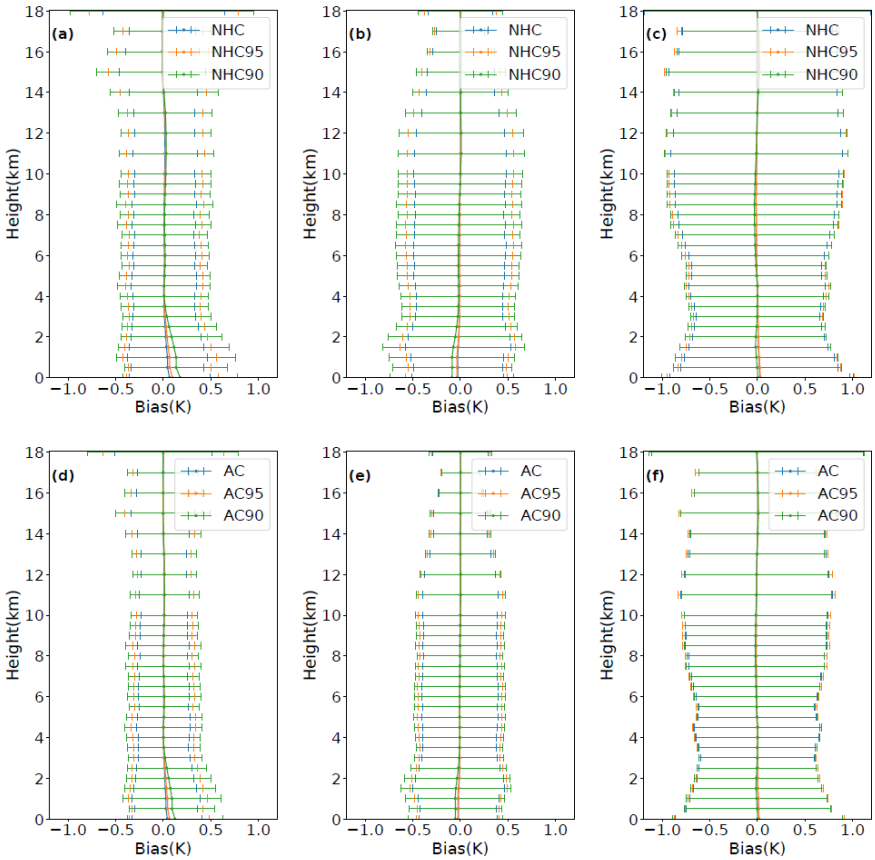

Figure 8. The statistical results of temperature profile retrieval errors for different channel configurations with only non-hyperspectral channels (upper row), and those including hyperspectral channels (bottom row). Columns from left to right correspond to clear, cloudy, and precipitating conditions. Error bars indicate RMSE.

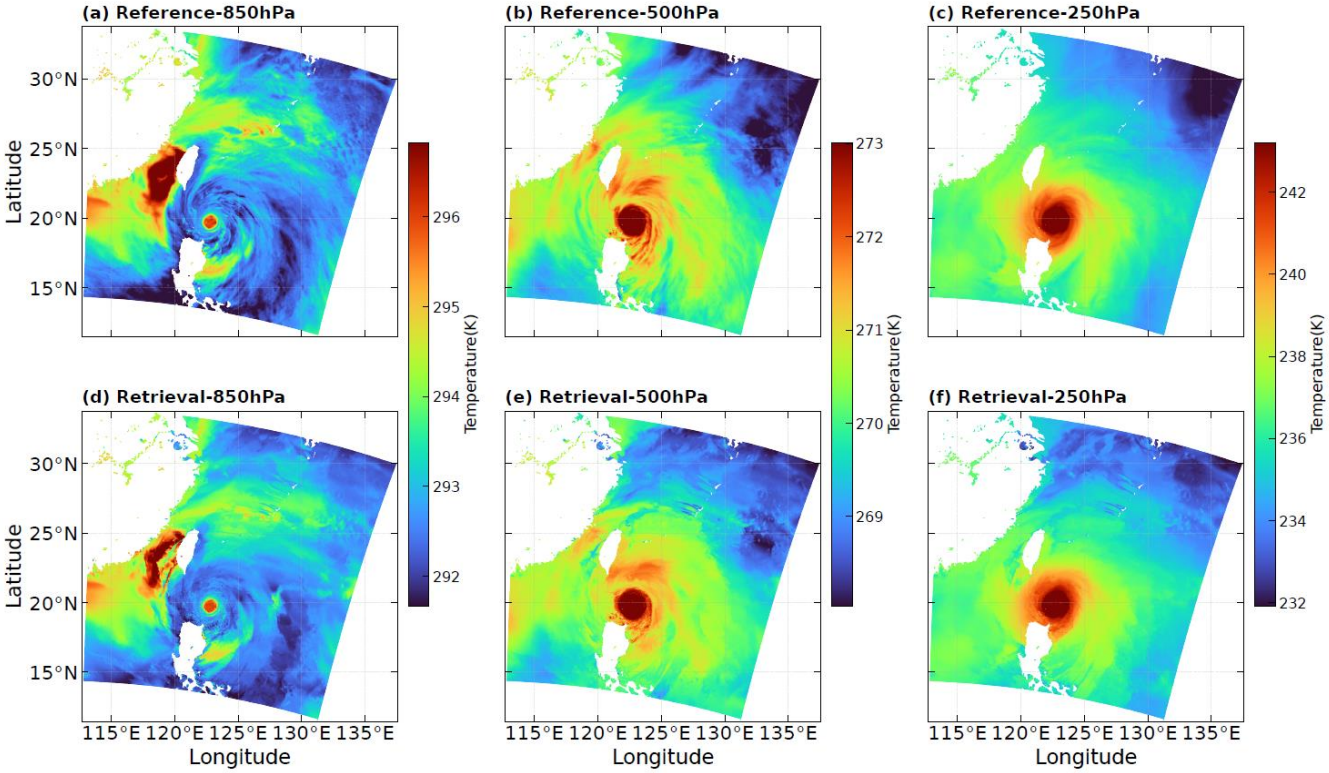

Figure 9. Spatial distributions of the simulated temperature fields by the WRF model (upper row), and retrieved temperature fields (bottom row) at different pressure levels (from left to right: 850 hPa, 500 hPa, and 250 hPa) for the Typhoon Doksuri case at 25 July 2023.

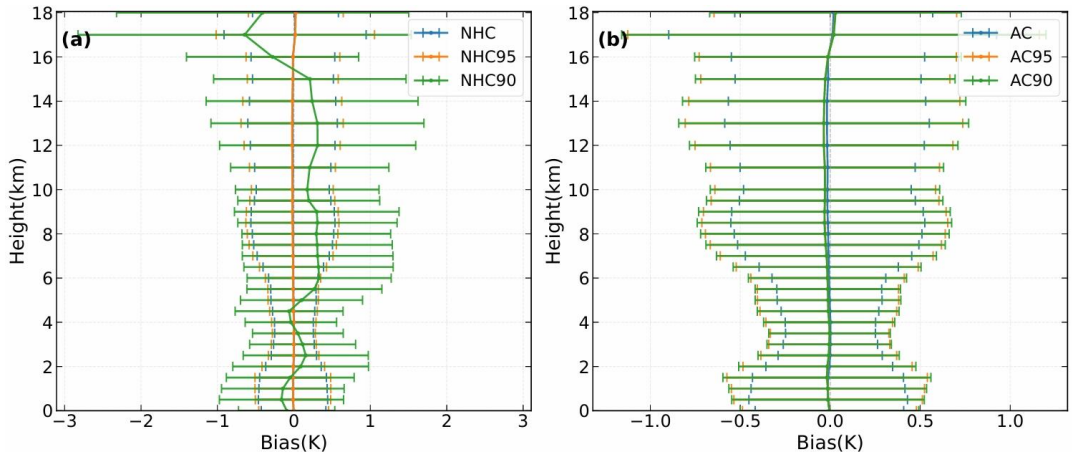

Figure 10. The statistical results of temperature profile retrieval errors for the typhoon case with (a) only non-hyperspectral channels and (b) all channels including hyperspectral channels. Error bars indicate RMSE.

Table 3. Retrieval calculation times of 100,000 samples for various channel configurations. The retrieval algorithms were performed on a supercomputing cluster node equipped with dual AMD EPYC 7702 processors. Each task was allocated 18 CPU cores and 1.8 GB of memory per core.

schemes	AC	AC95	AC90	NHC	NHC95	NHC90
time(s)	930	805	484	314	268	214

4 Conclusions and Discussion

As the world's first geostationary satellite carrying a passive microwave payload, the FY-4M satellite would open a new era of continuous three-dimensional observations of various key geophysical parameters associated with regional weather processes, featuring an unprecedented number of channels including hyperspectral channels of temperature sounding and multiple high-frequency channels being used for the first time. For the future operational system of this satellite, it is necessary to choose the appropriate channels from a total of 135 channels to achieve retrieval for different variables, in order to improve computational efficiency to cope with the maximum observation frequency of up to 3 minutes and to reduce observation errors or interference from redundant channels to enhance accuracy. In this study, channel optimization for temperature profile retrieval over ocean was performed based on information entropy theory, and the retrieval performance was evaluated using a Bayesian algorithm, thereby revealing the unique potential of the FY-4M satellite in all-sky and high-accuracy atmospheric temperature profile detection.

Based on the analysis of the Jacobian matrix, using degrees of freedom for signal (DFS) as the evaluation metric, channel optimization was performed via a sequential forward selection method based on information contribution ranking. The results show that in the absence of hyperspectral channels, the oxygen absorption bands at 50 GHz and 118 GHz are essential in atmospheric temperature sounding. However, once hyperspectral channels are introduced, the importance of these two bands would be significantly reduced. Instead, some water vapor and window channels (e.g., 23, 31, 89, and 183 GHz) become more important by providing information on water vapor, near-surface conditions, and hydrometeors, thereby playing a crucial role in constraining the atmospheric thermodynamic state. Based on the channel selection results, this study proposes an optimal channel configuration for atmospheric temperature profile retrieval, namely the AC95 scheme. It includes the hyperspectral channels (i.e., 52.7-57.3 GHz), along with selected channels mainly from water vapor absorption bands (i.e., 23 GHz, 183 GHz, and 380 GHz), and window channels (i.e., 31 GHz, 165 GHz, and 229 GHz).

To validate the accuracy and effectiveness of this optimized channel configuration scheme, atmospheric temperature profiles are retrieved based on the constructed a priori database. The validation results demonstrate that the inclusion of hyperspectral channels significantly improves the accuracy of temperature profile retrievals. For the AC95 configuration, the RMSE remains below 0.5 K under clear-sky and cloudy conditions, and is within 0.8 K during precipitating, which is clearly better than the results using all non-hyperspectral channels. In addition, the computational time is reduced by 14% relative to the full-channel configuration. Therefore, the proposed algorithm using AC95 configuration achieves a favorable balance between retrieval accuracy and computational efficiency, making it a preferred choice for future operational retrieval system.

Since the Bayesian framework can also be applied to the retrieval of other geophysical variables, future work will adopt this technique with a similar channel optimization strategy to obtain atmospheric humidity and various hydrometeor profiles, thereby providing more comprehensive three-dimensional information about the physical state of the atmosphere. In addition, to address the challenges of retrieving multiple parameters over land, efforts will be made to resolve the representation of complex land surface emissivity and then to construct a more accurate a priori database for channel optimization. On this basis, a complete operational retrieval system will be developed, enabling the FY-4M satellite to play a more important role in monitoring and forecasting typhoons, heavy precipitation, and other extreme weather events. Also, it should be noted that treating the hyperspectral band as a single superchannel effectively demonstrates the irreplaceable value of this band for temperature sounding, but the differences in information contribution among individual hyperspectral channels haven't been further quantified here. Future work will focus on channel selection within the hyperspectral band, with the aim of identifying the most critical sounding channels without substantially degrading retrieval accuracy.

Author contributions

Y.W.: Conceptualization, Methodology, Validation, Formal analysis, Writing - Original Draft, Project administration, Supervision, Funding acquisition. X.M.: Conceptualization, Methodology, Validation, Formal analysis, Software, Visualization, Writing - Original Draft. B.W.: Software. Q.G.: Review, Editing. J.X.: Writing - Original Draft. R.L., X.W., and X.L.: Review, Editing.

Competing interests

The authors declare that they have no competing interests.

Financial support

This work was supported by the Meteorological Joint Fund (grant No. U2542205) and Key program (grant No. 42330110) of the National Natural Science Foundation of China; Key program of Anhui Provincial Key Research and Development Project (grant No. 2408055UQ005); The China Meteorological Administration Science and Technology Project (grant No. CMAJBGS202502); China Meteorological Administration Xiong'an Atmospheric Boundary Layer Key Laboratory (grant No. 2025LABL-B09).

Data availability

The ERA5 hourly data on pressure levels and single levels used in this study are available from the Copernicus Climate Change Service Climate Data Store at https://doi.org/10.24381/cds.bd0915c6 and https://doi.org/10.24381/cds.adbb2d47, respectively (Copernicus Climate Change Service, Climate Data Store, 2023a, b). The GMI Level 1C-R Version 05 TB product is available at https://doi.org/10.5067/GPM/GMI/R/1C/05 (Berg, 2016), and the GMI Level 2 GPROF Version 07 product is available at https://doi.org/10.5067/GPM/GMI/GPROFCLIM/2A/07 (Kummerow, 2022).

References

Aires, F., Prigent, C., Orlandi, E., Milz, M., Eriksson, P., Crewell, S., Lin, C.-C., and Kangas, V.: Microwave hyperspectral measurements for temperature and humidity atmospheric profiling from satellite: the clear-sky case, J. Geophys. Res. Atmos., 120, 11334-11351, https://doi.org/10.1002/2015JD023331, 2015.

Aires, F., Prigent, C., Buehler, S. A., Eriksson, P., Milz, M., and Crewell, S.: Towards more realistic hypotheses for the information content analysis of cloudy/precipitating situations - application to a hyperspectral instrument in the microwave, Quart. J. Roy. Meteorol. Soc., 145, 1-14, https://doi.org/10.1002/qj.3315, 2019.

Berg, W.: GPM GMI_R Common Calibrated Brightness Temperatures Collocated L1C 1.5 h 13 km V05, Greenbelt, MD, USA, Goddard Earth Sciences Data and Information Services Center (GES DISC) [data set], https://doi.org/10.5067/GPM/GMI/R/1C/05 (last access: 24 August 2026), 2016.

Bi, Y., Yang, J., Wei, C., Dou, F., Xu, W., An, D., Luan, Y., Feng, J., and Zhang, L.: Atmospheric temperature measurements using microwave hyper-spectrum from geostationary satellite: band design, weighting functions and information content, Remote Sens., 16, 289, https://doi.org/10.3390/rs16020289, 2024.

Birman, C., Mahfouf, J. F., Milz, M., Mendrok, J., Buehler, S. A., and Brath, M.: Information content on hydrometeors from millimeter and sub-millimeter wavelengths, Tellus A Dyn. Meteorol. Oceanogr., 69, 1271562, https://doi.org/10.1080/16000870.2016.1271562, 2017.

Bormann, N., Geer, A., and English, S. J.: Evaluation of the microwave ocean surface emissivity model FASTEM-5 in the IFS, Eur. Centre Medium-Range Weather Forecasts, Reading, U.K., Tech. Memo. 667, https://doi.org/10.21957/l936s9df, 2012.

Chedin, A., Scott, N. A., Wahiche, C., and Moulinier, P.: The improved initialization inversion method: a high resolution physical method for temperature retrievals from satellites of the TIROS-N series, J. Appl. Meteor. Climatol., 24, 128-143, https://doi.org/10.1175/1520-0450(1985)024<0128:TIIIMA>2.0.CO;2, 1985.

Chen, K., Suo, Z., Han, W., and Cai, B.: OSSEs on the FY-4M geostationary microwave satellite based on CMA-GFS and CMA-MESO, IEEE Trans. Geosci. Remote Sens., 62, 5302819, https://doi.org/10.1109/TGRS.2024.3487859, 2024.

Chen, K., Suo, Z., Han, W., Cai, B., and Chen, Y.: Assessing the potential impact of microwave sounders on typhoon prediction using OSSEs: a comparative study between LEO constellation and GEO satellites, IEEE Geosci. Remote Sens. Lett., 22, 1-5, https://doi.org/10.1109/LGRS.2025.3548908, 2025.

Christensen, J., Carlstrom, A., Ekstrom, H., Emrich, A., Embretsén, J., and De Maagt, P.: GAS: The geostationary atmospheric sounder, in: Proc. IEEE Int. Geosci. Remote Sens. Symp. (IGARSS), Barcelona, Spain, 23-28 July 2007, 223-226, https://doi.org/10.1109/IGARSS.2007.4422770, 2007.

Copernicus Climate Change Service, Climate Data Store: ERA5 hourly data on pressure levels from 1940 to present, Copernicus Climate Change Service (C3S) Climate Data Store (CDS) [data set], https://doi.org/10.24381/cds.bd0915c6 (last access: 24 August 2026), 2023a.

Copernicus Climate Change Service, Climate Data Store: ERA5 hourly data on single levels from 1940 to present, Copernicus Climate Change Service (C3S) Climate Data Store (CDS) [data set], https://doi.org/10.24381/cds.adbb2d47 (last access: 24 August 2026), 2023b.

Draper, D. W., Newell, D. A., Wentz, F. J., Krimchansky, S., and Skofronick-Jackson, G. M.: The global precipitation measurement (GPM) microwave imager (GMI): instrument overview and early on-orbit performance, IEEE J. Sel. Topics Appl. Earth Observ. Remote Sens., 8, 3452-3462, https://doi.org/10.1109/JSTARS.2015.2403303, 2015.

Evans, K. F., Turk, J., Wong, T., and Stephens, G. L.: A Bayesian approach to microwave precipitation profile retrieval, J. Appl. Meteor. Climatol., 34, 260-279, https://doi.org/10.1175/1520-0450-34.1.260, 1995.

Gasiewski, A. J., Barrett, J. W., Bonanni, P. G., and Staelin, D. H.: Aircraft-based radiometric imaging of tropospheric temperature and precipitation using the 118.75-GHz oxygen resonance, J. Appl. Meteor. Climatol., 29, 620-632, https://doi.org/10.1175/1520-0450(1990)029<0620:ABRIOT>2.0.CO;2, 1990.

Gong, J. and Wu, D. L.: Microphysical properties of frozen particles inferred from Global Precipitation Measurement (GPM) Microwave Imager (GMI) polarimetric measurements, Atmos. Chem. Phys., 17, 2741-2757, https://doi.org/10.5194/acp-17-2741-2017, 2017.

He, J., Zhang, S. , and Wang, Z.: Advanced microwave atmospheric sounder (AMAS) channel specifications and T/V calibration results on FY-3C satellite, IEEE Trans. Geosci. Remote Sens., 53, 481-493, https://doi.org/10.1109/TGRS.2014.2324173, 2015.

He, W., Chen, H., Xuan, Y., Li, J., Duan, M., and Nan, W.: Ground mobile observation system for measuring multisurface microwave emissivity, Atmos. Meas. Tech., 14, 7069-7078, https://doi.org/10.5194/amt-14-7069-2021, 2021.

He, W., Xia, X., Wu, S., Zhang, P., Chen, H., Xia, X., Zhou, Y., and Cai, M.: A rapid assessment of MWRI-RM/FY3G brightness temperature, Atmos. Ocean. Sci. Lett., 17, 100466, https://doi.org/10.1016/j.aosl.2024.100466, 2024.

Hersbach, H., Bell, B., Berrisford, P., Hirahara, S., Horányi, A., Muñoz-Sabater, J., Nicolas, J., Peubey, C., Radu, R., Schepers, D., Simmons, A., Soci, C., Abdalla, S., Abellan, X., Balsamo, G., Bechtold, P., Biavati, G., Bidlot, J., Bonavita, M., De Chiara, G., Dahlgren, P., Dee, D., Diamantakis, M., Dragani, R., Flemming, J., Forbes, R., Fuentes, M., Geer, A., Haimberger, L., Healy, S., Hogan, R. J., Hólm, E., Janisková, M., Keeley, S., Laloyaux, P., Lopez, P., Lupu, C., Radnoti, G.,

de Rosnay, P., Rozum, I., Vamborg, F., Villaume, S., and Thépaut, J.-N.: The ERA5 global reanalysis, Quart. J. Roy. Meteorol. Soc., 146, 1999-2049, https://doi.org/10.1002/qj.3803, 2020.

Hu, J., Li, R., Zhang, P., Wang, Y., Wu, S., Letu, H., and Weng, F.: Global retrieval of harmonized microwave land surface emissivity leveraging multi-sensor measurements from GMI, AMSR2 and MWRIs, Remote Sens. Environ., 334, 115169, https://doi.org/10.1016/j.rse.2025.115169, 2026.

Koshelev, M. A., Vilkov, I. N., Makarov, D. S., Tretyakov, M. Yu., Vispoel, B., Gamache, R. R., Cimini, D., Romano, F., and Rosenkranz, P. W.: Water vapor line profile at 183-GHz: Temperature dependence of broadening, shifting, and speed-dependent shape parameters, J. Quant. Spectrosc. Radiat. Transfer, 262, 107472, https://doi.org/10.1016/j.jqsrt.2020.107472, 2021.

Kummerow, C., Berg, W., Thomas-Stahle, J., and Masunaga, H.: Quantifying global uncertainties in a simple microwave rainfall algorithm, J. Atmos. Oceanic Technol., 23, 23-37, https://doi.org/10.1175/JTECH1827.1, 2006.

Kummerow, C. D., Ringerud, S., Crook, J., Randel, D., and Berg, W.: An observationally generated a priori database for microwave rainfall retrievals, J. Atmos. Oceanic Technol., 28, 113-130, https://doi.org/10.1175/2010JTECHA1468.1, 2011.

Kummerow, C. D., Randel, D. L., Kulie, M., Wang, N.-Y., Ferraro, R., Munchak, S. J., and Petkovic, V.: The evolution of the Goddard profiling algorithm to a fully parametric scheme, J. Atmos. Oceanic Technol., 32, 2265-2280, https://doi.org/10.1175/JTECH-D-15-0039.1, 2015.

Kummerow, C. D., Poczatek, J. C., Almond, S., Berg, W., Jarrett, O., Jones, A., Kantner, M., and Kuo, C. P.: Hyperspectral microwave sensors—Advantages and limitations, IEEE J. Sel. Topics Appl. Earth Observ. Remote Sens., 15, 764-775, https://doi.org/10.1109/JSTARS.2021.3133382, 2022.

Kummerow, C.: GPM GMI (GPROF) Climate-based Radiometer Precipitation Profiling L2A 1.5 h 4 km × 4 km V07, Greenbelt, MD, USA, Goddard Earth Sciences Data and Information Services Center (GES DISC) [data set], https://doi.org/10.5067/GPM/GMI/GPROFCLIM/2A/07 (last access: 24 August 2026), 2022.

Lambrigtsen, B., Tanner, A., Gaier, T., Kangaslahti, P., and Brown, S.: Prototyping a new earth observing sensor—GeoSTAR, in: Proc. IEEE Aerosp. Conf., Big Sky, Montana, USA, 3-10 March 2007, 1-9, https://doi.org/10.1109/AERO.2007.352690, 2007.

Lambrigtsen, B., Gaier, T., Kangaslahti, P., Lim, B., Tanner, A., and Ruf, C.: Enabling the NASA decadal–survey “PATH” mission, in: Proc. IEEE Int. Geosci. Remote Sens. Symp. (IGARSS), Beijing, China, 10-15 July 2016, 3949-3951, https://doi.org/10.1109/IGARSS.2016.7730026, 2016.

Lawrence, H., Carminati, F., Bell, W., Bormann, N., Newman, S., Atkinson, N., Geer, A., Migliorini, S., Lu, Q., and Chen, K.: An evaluation of FY-3C MWRI and assessment of the long-term quality of FY-3C MWHS-2 at ECMWF and the Met Office, Eur. Centre Medium-Range Weather Forecasts, Reading, UK, Tech. Memo. 798, https://doi.org/10.21957/lhuph6fb3, 2017.

Li, R., Wang, Y., Hu, J., Wang, Y., Min, Q., Bergeron, Y., Valeria, O., Gao, Z., Liu, J., and Fu, Y.: Spatiotemporal variations of satellite microwave emissivity difference vegetation index in China under clear and cloudy skies, Earth Space Sci., 7, e2020EA001145, https://doi.org/10.1029/2020ea001145, 2020.

Li, R., Hu, J., Wu, S., Zhang, P., Letu, H., Wang, Y., Wang, X., Fu, Y., Zhou, R., and Sun, L.: Spatiotemporal variations of microwave land surface emissivity (MLSE) over China derived from four-year recalibrated Fengyun 3B MWRI data, Adv. Atmos. Sci., 39, 1536-1560, https://doi.org/10.1007/s00376-022-1314-0, 2022.

Liu, G.: A fast and accurate model for microwave radiance calculations, J. Meteorol. Soc. Jpn., 76, 335-343, https://doi.org/10.2151/jmsj1965.76.2_335, 1998.

Liu, Q., Weng, F., and English, S. J.: An improved fast microwave water emissivity model, IEEE Trans. Geosci. Remote Sens., 49, 1238-1250, https://doi.org/10.1109/TGRS.2010.2064779, 2011.

Liu, S., Xu, J., Chen, L., Liu, H., Wang, W., He, J., Zhu, S., and Shi, J.: Comprehensive validation of temperature and humidity profile retrievals from FengYun-3E, IEEE Trans. Geosci. Remote Sens., 64, 4102214, https://doi.org/10.1109/TGRS.2026.3658572, 2026.

Mahfouf, J.-F., Birman, C., Aires, F., Prigent, C., Orlandi, E., and Milz, M.: Information content on temperature and water vapour from a hyper-spectral microwave sensor, Quart. J. Roy. Meteorol. Soc., 141, 3268-3284, https://doi.org/10.1002/qj.2608, 2015.

Mech, M., Maahn, M., Kneifel, S., Ori, D., Orlandi, E., Kollias, P., Schemann, V., and Crewell, S.: PAMTRA 1.0: The Passive and Active Microwave radiative TRAnsfer tool for simulating radiometer and radar measurements of the cloudy atmosphere, Geosci. Model Dev., 13, 4229-4251, https://doi.org/10.5194/gmd-13-4229-2020, 2020.

Mo, T., Goldberg, M. D., Crosby, D. S., and Cheng, Z.: Recalibration of the NOAA microwave sounding unit, J. Geophys. Res. Atmos., 106, 10145-10150, https://doi.org/10.1029/2001JD900027, 2001.

Rodgers, C. D.: Information content and optimisation of high spectral resolution remote measurements, Adv. Space Res., 21, 361-367, https://doi.org/10.1016/S0273-1177(97)00915-0, 1998.

Rodgers, C. D.: Inverse methods for atmospheric sounding: Theory and practice, World Scientific, Singapore, https://doi.org/10.1142/3171, 2000.

Sahoo, S., Bosch-Lluis, X., Reising, S. C., and Vivekanandan, J.: Radiometric information content for water vapor and temperature profiling in clear skies between 10 and 200 GHz, IEEE J. Sel. Topics Appl. Earth Observ. Remote Sens., 8, 859-871, https://doi.org/10.1109/JSTARS.2014.2364394, 2015.

Tretyakov, M. Y., Parshin, V. V., Shanin, V. N., Myasnikova, S. E., Koshelev, M. A., and Krupnov, A. F.: Real atmosphere laboratory measurements of the 118-GHz oxygen line: Shape, shift, and broadening of the line, J. Mol. Spectrosc., 208, 110-112, https://doi.org/10.1006/jmsp.2001.8363, 2001.

Wang, D., Tong, L., Gong, X., Guan, X., Wang, P., and Gao, B.: Retrieval of atmospheric temperature profiles from hyperspectral microwave radiative data based on the neural network, in: Proc. IEEE Int. Geosci. Remote Sens. Symp. (IGARSS), Brussels, Belgium, 11–16 July 2021, 7095-7098, https://doi.org/10.1109/IGARSS47720.2021.9554282, 2021.

Weng, F., Zhao, L., Ferraro, R. R., Poe, G., Li, X., and Grody, N. C.: Advanced microwave sounding unit cloud and precipitation algorithms, Radio Sci., 38, 8068, https://doi.org/10.1029/2002RS002679, 2003.

Weng, F., Zou, X., Sun, N., Yang, H., Tian, M., Blackwell, W. J., Wang, X., Lin, L., and Anderson, K.: Calibration of Suomi national polar-orbiting partnership advanced technology microwave sounder, J. Geophys. Res. Atmos., 118, 11187-11200, https://doi.org/10.1002/jgrd.50840, 2013.

Wentz, F. J. and Draper, D.: On-orbit absolute calibration of the Global Precipitation Measurement Microwave Imager, J. Atmos. Oceanic Technol., 33, 1393-1412, https://doi.org/10.1175/JTECH-D-15-0212.1, 2016.

Wu, B., Li, X., Wang, Y., Fan, X., Zhang, P., Chen, L., and Fu, Y.: A prototype precipitation retrieval algorithm for passive microwave observations from the FY-3G satellite, J. Remote Sens., 6, 1057, https://doi.org/10.34133/remotesensing.1057, 2026.

Xiao, X. and Weng, F.: A comparison of information content at microwave to millimeter wave bands for atmospheric sounding, Remote Sens., 14, 6124, https://doi.org/10.3390/rs14236124, 2022.

Xie, Z., Li, X., Yao, C., Jiang, L., and Li, X.: Research on geostationary orbit microwave radiometer technology, Aerosp. Shanghai, 35, 20-28, https://doi.org/10.19328/j.cnki.1006-1630.2018.02.003, 2018a.

Xie, Z., Xu, H., An, D., He, J., Zhang, D., and Zhu, Z.: Remote sensing technology of experimental microwave radiometer in geostationary orbit, Aerosp. Shanghai, 35, 49-59, https://doi.org/10.19328/j.cnki.1006.1630.2018.02.006, 2018b.

Xue, Q., Guan, L., and Shi, X.: One-dimensional variational retrieval of temperature and humidity profiles from the FY4A GIIRS, Adv. Atmos. Sci., 39, 471-486, https://doi.org/10.1007/s00376-021-1032-z, 2022.

Yan, X., Liang, C., Jiang, Y., Luo, N., Zang, Z., and Li, Z.: A deep learning approach to improve the retrieval of temperature and humidity profiles from a ground-based microwave radiometer, IEEE Trans. Geosci. Remote Sens., 58, 8427-8437, https://doi.org/10.1109/TGRS.2020.2987896, 2020.

Yang, H., Chen, Z., Sun, S., Li, M., Cai, W., Wu, L., Cai, J., Sun, B., Ma, K., and Ma, X.: Observations reveal intense air-sea exchanges over submesoscale ocean front, Geophys. Res. Lett., 51, e2023GL106840, https://doi.org/10.1029/2023GL106840, 2024.

Yin, M. and Liu, G.: Developing an a priori database for passive microwave snow water retrievals over ocean, J. Geophys. Res. Atmos., 122, 12960-12981, https://doi.org/10.1002/2017JD027636, 2017.

Zhang, L., Ma, Y., Lei, L., Wang, Y., Jin, S., and Gong, W.: Improving atmospheric temperature and relative humidity profiles retrieval based on ground-based multichannel microwave radiometer and millimeter-wave cloud radar, Atmosphere, 15, 1064, https://doi.org/10.3390/atmos15091064, 2024.

Zhang, P., Xu, Z., Guan, M., Xie, L., Xian, D., and Liu, C.: Progress of Fengyun meteorological satellites since 2020, Chinese J. Space Sci., 42, 724-732, https://doi.org/10.11728/cjss2022.04.yg14, 2022.

Zhang, P., Gu, S., Chen, L., Shang, J., Lin, M., Zhu, A., Yin, H., Wu, Q., Shou, Y., Sun, F., Xu, H., Yang, G., Wang, H., Li, L., Zhang, H., Chen, S., and Lu, N.: FY-3G satellite instruments and precipitation products: First report of China's Fengyun rainfall mission in-orbit, J. Remote Sens., 3, 0097, https://doi.org/10.34133/remotesensing.0097, 2023.

Zhou, L., Lei, L., Whitaker, J. S., and Tan, Z.-M.: An adaptive channel selection method for assimilating the hyperspectral infrared radiances, Mon. Weather Rev., 152, 793-810, https://doi.org/10.1175/MWR-D-23-0131.1, 2024.